VELOCITY AND ACCELERATION ESTIMATION OF DOPPLER WEATHER RADAR/LIDAR SIGNALS IN COLORED NOISE

Weige Chen *Guotong Zhou* *Georgios B. Giannakis*
Department of Electrical Engineering, University of Virginia, Charlottesville, VA 22903-2442, USA

ABSTRACT

We are interested in estimating the Doppler shift occurred in weather radar returns, which yields precipitation velocity information. Conventional techniques including the pulse pair processor rely heavily on the assumption that the additive noise is white and hence their performance degrades when the noise color is unknown. Because the data length for a given range gate is usually small, we employ the high resolution MUSIC algorithm to estimate the Doppler shift. The challenge lies not only in proving that MUSIC is applicable to weather radar signals which are affected by multiplicative noise, but also in showing that MUSIC is robust when the additive noise is colored. The resulting algorithm can also be used to infer wind speed from a small number of lidar observations where the velocity is approximately constant. Assuming linear shear over a longer range, we employ the ambiguity function to estimate the acceleration and instantaneous wind velocity. Real weather radar and lidar data as well as simulated examples are provided to illustrate the performance of the algorithms.

1. INTRODUCTION

Doppler radar has become the primary tool of measuring precipitation (rain or snow) in a large area. It operates by transmitting microwave pulses to the atmosphere and processing the returned signals. Atmospheric scatterers of microwave pulses are hydrometeors which contain precipitation information. The backscattered wave is then picked up by the antenna and converted into digital samples.

The returned signal for a given range gate is modeled in discrete-time as [3, p. 124],

$$x(t) = s(t)\, e^{j\omega_0 t} + v(t), \quad t = 0, 1, \ldots, N-1, \qquad (1)$$

where $s(t)$ and $v(t)$ are assumed to be zero-mean, circular complex Gaussian processes. Multiplicative noise $s(t)$ is assumed to have a bell-shaped power spectral density (PSD) which is narrowband and centered at zero frequency. Additive noise $v(t)$ is assumed to be white. The Doppler shift ω_0 (in rads/sec) is proportional to the speed at which the scatterers are moving relative to the receiver.

The random amplitude model in (1) is adopted because there is a large number of scatterers in a resolution volume (typical dimension in the order of hundreds of meters), and the received signal is a superposition of waves from all these scatterers. Due to wind shear or turbulence, the scatterers move relative to each other, have random positions, and random phases. Such incoherence broadens the signal spectrum. The additive noise $v(t)$ is due to shot noise in the receiver and cosmic noise.

The covariance of (1) is given by

$$r_x(\tau) := E[x^*(t)x(t+\tau)] = r_s(\tau)\, e^{j\omega_0\tau} + r_v(\tau), \qquad (2)$$

where $r_s(\tau)$ and $r_v(\tau)$ are the covariances of $s(t)$ and $v(t)$ respectively. Because the PSD of $s(t)$ is symmetric w.r.t. the zero frequency, $r_s(\tau)$ is real. Moreover, if $v(t)$ is white, $r_v(\tau) = 0$, $\tau \neq 0$. Therefore, we have that

$$\omega_0 = \arg[r_x(1)]. \qquad (3)$$

Sample estimate of (3) is obtained via

$$\hat{\omega}_0 = \arg\left[\frac{1}{N}\sum_{t=0}^{N-1} x^*(t)x(t+1)\right]. \qquad (4)$$

The estimator in (4) is the so-called pulse-pair (PP) processor [3, Ch. 6], which is the dominant technique used by weather radar practitioners to infer rainfall speed.

However, the accuracy of the PP processor relies heavily on the modeling assumptions and as we show in Section 4, significant error occurs when $v(t)$ is non-white (colored).

The Fourier transform (FT) of (2) yields the PSD,

$$S_x(\omega) := \sum_{\tau=-\infty}^{\infty} r_x(\tau)\, e^{-j\omega\tau} = S_s(\omega - \omega_0) + S_v(\omega). \qquad (5)$$

Under the modeling assumptions of (1), the PSD of $x(t)$ is bell-shaped centered at ω_0 and is superimposed on a flat background due to $v(t)$. However, as reported in [6], 25% of the actual precipitation spectra deviate significantly from this model. Anomalies include asymmetric spectra and spectra exhibiting multiple peaks.

In [7], it is also observed that $S_x(\omega)$ may exhibit "a significant though relatively weak secondary peak that is clearly separated from the main peak," and that "the co-existence of widely separated peaks will cause biases in the Doppler shift estimates of the desired signal." A means of modeling the additional peak(s) is to allow $v(t)$ to be colored.

In Section 2 of this paper, we extend the popular MUSIC algorithm [4, Sec. 12.3] for constant amplitude harmonic retrieval to the random amplitude model in (1), and demonstrate its superiority over the PP processor especially when $v(t)$ is colored.

Although Doppler radar is a useful tool to "see through" a storm and measure wind velocity inside, it is not as powerful as Doppler lidar for measuring wind under clear air conditions. The principle of Doppler lidar is similar to that of Doppler radar, except that microwave pulses are replaced by laser beams, and scatterers are atmospheric aerosol particles instead of hydrometeors.

Reliable wind estimation is important not only for improving weather forecast accuracy, but also for planning and controlling spacecraft landing. In addition, the ability to detect low altitude wind shear conditions such as microbursts is crucial to aircraft safety.

Although lidar and radar operate differently, the same model (1) has been adopted for lidar returns [8]. In radar,

0-7803-2431-5/95 $4.00

all N samples are due to the scatterers in the same resolution volume, and hence ω_0 can be regarded as approximately constant. For lidar however, successive samples of $x(t)$ correspond to overlapping but different resolution volumes, and hence only over a limited number of samples, ω_0 can be regarded as approximately constant. In general, ω_0 changes with t, and a larger t corresponds to increasing distance and height. It is known that due to decreasing surface friction, the average wind speed tends to increase linearly with height (linear shear). In Section 3, we model lidar returns as random amplitude modulated chirp signals, and employ the ambiguity function to estimate wind acceleration and instantaneous velocity. Such information could be useful to identify potentially hazardous shear zones. The performance of the algorithms is illustrated in Section 4 based on simulated as well as observed weather signals.

2. MUSIC IN COLORED NOISE

The MUSIC algorithm [4, Sec. 12.3] has become a benchmark algorithm for retrieving *constant* amplitude harmonics in additive *white* noise, especially when the data length is small and hence FFT based approaches have poor resolution. The objective of this section is to show that at least for a single harmonic, MUSIC is applicable when $v(t)$ is colored, and when multiplicative noise is also present.

First, let us define $(K+1)\times 1$ vectors $\mathbf{x}(t) := [x(t)\ x(t+1)\ \ldots\ x(t+K)]^T$, and $\mathbf{v}(t) := [v(t)\ v(t+1)\ \ldots\ v(t+K)]^T$, where ^{T} stands for transpose. The assumption that $s(t)$ is narrowband and lowpass ensures that $s(t)$ does not fluctuate much within a processing window of length $K+1$, which in turn, allows us to write

$$\mathbf{s}(t) := [1\ e^{j\omega_0}\ \ldots\ e^{jK\omega_0}]^T s(t)\, e^{j\omega_0 t} := \mathbf{e}(\omega_0)\, s(t)\, e^{j\omega_0 t}. \quad (6)$$

Next, let us define $\mathbf{R}_x := E[\mathbf{x}(t)\mathbf{x}^H(t)]$ to be the correlation matrix of $\mathbf{x}(t)$, where ^{H} denotes Hermitian. Similar definitions hold for $\mathbf{R}_s$ and $\mathbf{R}_v$. Due to the zero-mean and independence of $s(t)$ and $v(t)$, we obtain via (6)

$$\mathbf{R}_x = \mathbf{R}_s + \mathbf{R}_v = \sigma_s^2 \mathbf{e}(\omega_0)\mathbf{e}^H(\omega_0) + \mathbf{R}_v,\ \sigma_s^2 := E[|s(t)|^2], \quad (7)$$

Let $\lambda_i(\mathbf{R})$ denote the ith eigenvalue of $\mathbf{R}$ and assume w.l.o.g. that $\lambda_{i+1}(\mathbf{R}) \geq \lambda_i(\mathbf{R})$; i.e., in ascending order.

For the constant amplitude harmonic in additive white noise model, $x(t) = A\exp\{j\omega_0 t\} + v(t)$, we find $\mathbf{R}_x = A^2\, \mathbf{e}(\omega_0)\, \mathbf{e}^H(\omega_0) + \sigma_v^2\, \mathbf{I}$. It follows that $\mathbf{e}(\omega_0)$ is an eigenvector of $\mathbf{R}_x$ with corresponding eigenvalue $\lambda_{K+1}(\mathbf{R}_x) = (K+1)A^2 + \sigma_v^2$. Since the rest K eigenvectors $\{\mathbf{q}_i\}_{i=1}^K$ of $\mathbf{R}_x$ must be orthogonal to $\mathbf{e}(\omega_0)$, it follows that $\lambda_i(\mathbf{R}_x) = \sigma_v^2$, $i \in [1, K]$. Therefore, by eigen-decomposing $\mathbf{R}_x$ and identifying the eigenvectors corresponding to the least K eigenvalues of $\mathbf{R}_x$, which are not affected by the signal, one finds the so-called noise subspace, $\mathbf{Q} := [\mathbf{q}_1\ \ldots\ \mathbf{q}_K]$. Because $\mathbf{R}_x\mathbf{q}_i = \sigma_v^2\mathbf{q}_i$, we find that $A^2\ \mathbf{e}(\omega_0)\ \mathbf{e}^H(\omega_0)\ \mathbf{q}_i = \mathbf{0}$, and hence $\mathbf{e}(\omega_0) \perp \mathbf{q}_i$, $i \in [1, K]$, or, $\mathbf{e}(\omega_0) \perp \mathbf{Q}$. If one computes

$$f(\omega) := \mathbf{e}^H(\omega)\mathbf{Q}\mathbf{Q}^H\mathbf{e}(\omega),\ \ \mathbf{e}(\omega) := [1\ e^{j\omega}\ \ldots\ e^{jK\omega}]^T, \quad (8)$$

and plots the so-called MUSIC pseudo-spectrum $1/f(\omega)$ for $\omega \in [-\pi, \pi)$, then a sharp peak occurs at ω_0.

The preceding analysis does not go through when $v(t)$ is colored. However, we recognize that the key effects of the noise color are in disturbing: (k1) identification of the noise subspace; and (k2) the orthogonality. The following assumption is made to cope with (k1): **(a1)** $S_v(\omega)$ is smooth. This is easily met by all stationary and mixing [1, p. 9] processes. In addition, we assume **(a2)** $\sigma_s^2 \gg \max_\omega S_v(\omega)$, which helps us to approximate (k2) when $v(t)$ is colored. Note that **(a2)** amounts to a high SNR requirement.

The following interlacing theorem w.r.t. (7) is useful:

Theorem 1 [5, p. 182-183]: *If the eigenvalues of* $\mathbf{R}_v$ *and* $\mathbf{R}_x$ *are arranged in non-decreasing order, then it holds that*

$$\lambda_i(\mathbf{R}_v) \leq \lambda_{i+1}(\mathbf{R}_x) \leq \lambda_{i+2}(\mathbf{R}_v),\ \ i \in [1, K-1]. \quad (9)$$

According to (9), we find,

$$\lambda_1(\mathbf{R}_v) \leq \lambda_2(\mathbf{R}_x) \leq \ldots \leq \lambda_K(\mathbf{R}_x) \leq \lambda_{K+1}(\mathbf{R}_v). \quad (10)$$

The next theorem gives bounds on the smallest and the largest eigenvalues of $\mathbf{R}_x$ in terms of those of $\mathbf{R}_v$.

Theorem 2 [5, p. 184]: *Let* $\mathbf{R}_s$, $\mathbf{R}_v$, $\mathbf{R}_x = \mathbf{R}_s + \mathbf{R}_v$ *be Hermitian matrices, with the eigenvalues arranged in non-decreasing order. Then for* $1 \leq l, i \leq K+1$, $l+i \leq K+2$,

$$\lambda_{l+i-1}(\mathbf{R}_x) \geq \lambda_l(\mathbf{R}_v) + \lambda_i(\mathbf{R}_s). \quad (11)$$

Since $\mathbf{R}_s$ of (7) has $\lambda_{K+1}(\mathbf{R}_s) = (K+1)\sigma_s^2$, and $\lambda_i(\mathbf{R}_s) = 0$ for $i \in [1, K]$, it follows easily from Theorem 2 that

$$\lambda_1(\mathbf{R}_x) \geq \lambda_1(\mathbf{R}_v), \quad (12)$$

$$\lambda_{K+1}(\mathbf{R}_x) \geq \max\{\lambda_{K+1}(\mathbf{R}_v), \lambda_1(\mathbf{R}_v) + (K+1)\sigma_s^2\}. \quad (13)$$

Combining (10) and (12), we see that the K least eigenvalues of $\mathbf{R}_x$ are restricted to within $[\lambda_1(\mathbf{R}_v),\ \lambda_{K+1}(\mathbf{R}_v)]$. Additionally, a result of [1, p. 74] indicates that under **(a1)**, the (perhaps re-ordered) eigenvalues of $\mathbf{R}_v$ tend to $S_v(\omega)$ at $\omega = 2\pi l/(K+1)$, for $l \in [1, K+1]$. Because $S_v(\omega)$ is smooth, we infer that the eigenvalues of $\mathbf{R}_v$, and hence $\lambda_i(\mathbf{R}_x)$, $i \in [1, K]$, lie close together, and are not affected much by the signal. Moreover, (13) indicates that the largest eigenvalue of $\mathbf{R}_x$ is well separated from the rest. Therefore, $\mathbf{Q} := [\mathbf{q}_1\ \ldots\ \mathbf{q}_K]$ gives rise to the "noise subspace", where $\{\mathbf{q}_i\}_{i=1}^K$ correspond to the K least eigenvalues of $\mathbf{R}_x$.

To assess the orthogonality between $\mathbf{e}(\omega_0)$ and $\mathbf{Q}$, let $\mathbf{q}_i$ be normalized. In the sequel, we shall use $\|\cdot\|$ to denote both the vector and matrix norms. For vectors, it is the ℓ_2 norm [5, p. 283], whereas for matrices, it is the spectral norm [5, p. 295], defined for square matrices as the maximum absolute eigenvalue.

It follows from (7) that

$$\mathbf{R}_s\mathbf{q}_i = \mathbf{R}_x\mathbf{q}_i - \mathbf{R}_v\mathbf{q}_i = \left[\lambda_i(\mathbf{R}_x)\mathbf{I} - \mathbf{P}^H\mathbf{D}(\mathbf{R}_v)\mathbf{P}\right]\mathbf{q}_i, \quad (14)$$

where $\mathbf{P}$ denotes the unitary eigenvector matrix of $\mathbf{R}_v$ and $\mathbf{D}(\mathbf{R}_v)$ is the diagonal matrix consisting of the eigenvalues of $\mathbf{R}_v$. Next, we infer from (14) that for $\forall i \in [1, K]$,

$$\|\mathbf{R}_s\mathbf{q}_i\| \leq \|\lambda_i(\mathbf{R}_x)\mathbf{I} - \mathbf{D}(\mathbf{R}_v)\| = \max_l\{|\lambda_i(\mathbf{R}_x) - \lambda_l(\mathbf{R}_v)|\}. \quad (15)$$

From (10) and (12), it follows that $\lambda_1(\mathbf{R}_v) \leq \lambda_i(\mathbf{R}_x) \leq \lambda_{K+1}(\mathbf{R}_v)$, $\forall i \in [1, K]$. Hence, we have $|\lambda_i(\mathbf{R}_x) - \lambda_l(\mathbf{R}_v)| \leq |\lambda_1(\mathbf{R}_v) - \lambda_{K+1}(\mathbf{R}_v)|$. Additionally, it is known that all eigenvalues of $\mathbf{R}_v$ are bounded by the minimum and maximum of $S_v(\omega)$ [4, p. 140]; we thus rewrite (15) as

$$\|\mathbf{R}_s\mathbf{q}_i\| \leq \left[\max_\omega S_v(\omega) - \min_\omega S_v(\omega)\right]. \quad (16)$$

Furthermore, we obtain from (7) and (16) that

$$\|\mathbf{e}(\omega_0)\mathbf{e}^H(\omega_0)\mathbf{q}_i\| \leq \frac{1}{\sigma_s^2}\ \left[\max_\omega S_v(\omega) - \min_\omega S_v(\omega)\right]. \quad (17)$$

Under **(a2)** and based on (17), we have $\|\mathbf{e}(\omega_0)\ \mathbf{e}^H(\omega_0)\ \mathbf{q}_i\| \approx 0$, which holds only when $\mathbf{e}^H(\omega_0)\ \mathbf{q}_i \approx 0$, $i \in [1, K]$, or, $\mathbf{e}^H(\omega_0)\mathbf{Q} \approx \mathbf{0}$. This concludes our analysis of the approximate orthogonality condition in a colored $v(t)$ scenario. As in the constant amplitude case, the MUSIC

pseudo-spectrum is defined as $1/f(\omega)$, where $f(\omega)$ is given by (8). The maximum of $1/f(\omega)$, or, the minimum of $f(\omega)$ yields $\hat{\omega}_0$ as the MUSIC frequency estimate.

Next, we wish to establish a bound on the error $\hat{\omega}_0 - \omega_0$, which is due to colored $v(t)$. The Taylor series expansion of (8) around $\hat{\omega}_0$, with $f'(\hat{\omega}_0) = 0$ and $f(\hat{\omega}_0) \geq 0$, yields:

$$f(\omega_0) \approx f(\hat{\omega}_0) + \frac{1}{2} f''(\hat{\omega}_0)(\omega_0 - \hat{\omega}_0)^2 \geq \frac{1}{2} f''(\hat{\omega}_0)(\omega_0 - \hat{\omega}_0)^2. \tag{18}$$

Since $\|\mathbf{e}(\omega_0)\mathbf{e}^H(\omega_0)\mathbf{q}_i\| = \|\mathbf{e}(\omega_0)\|\ |\mathbf{e}^H(\omega_0)\mathbf{q}_i| = \sqrt{K+1}\ |\mathbf{e}^H(\omega_0)\mathbf{q}_i|$, we have from (17) that for $i \in [1, K]$,

$$|\mathbf{e}^H(\omega_0)\mathbf{q}_i| \leq \frac{\max_\omega S_v(\omega) - \min_\omega S_v(\omega)}{\sqrt{K+1}\,\sigma_s^2}. \tag{19}$$

The quadratic function in (8) can be written as $f(\omega_0) = \sum_{i=1}^{K} |\mathbf{e}^H(\omega_0)\mathbf{q}_i|^2$, and based on (18) and (19), we obtain:

$$|\omega_0 - \hat{\omega}| \leq \sqrt{\frac{2K}{(K+1)f''(\hat{\omega}_0)}}\ \frac{\max_\omega S_v(\omega) - \min_\omega S_v(\omega)}{\sigma_s^2}, \tag{20}$$

$$f''(\hat{\omega}_0) = 2\mathrm{Re}[\mathbf{e}'^H(\hat{\omega}_0)\mathbf{Q}\mathbf{Q}^H\mathbf{e}'(\hat{\omega}_0) + \mathbf{e}^H(\hat{\omega}_0)\mathbf{Q}\mathbf{Q}^H\mathbf{e}''(\hat{\omega}_0)].$$

We observe the following w.r.t. (20): i) Its r.h.s. is zero when $v(t)$ is white, and hence $\hat{\omega}_0$ is theoretically error-free (recall that throughout Section 2 we have ignored finite sample effects); ii) The less fluctuation in $S_v(\omega)$, the smaller the error. This is intuitively true since a peaky $S_v(\omega)$ may confuse the algorithm to treat $v(t)$ as a random amplitude harmonic; iii) The error decreases when the SNR increases.

3. ACCELERATION ESTIMATION

As mentioned in the introduction, the Doppler shift cannot be regarded as constant over a long range in lidar applications. This prompts us to remodel $x(t)$, under the linear shear condition, as a random amplitude chirp signal,

$$x(t) = s(t)\ e^{j(a_2 t^2 + a_1 t)} + v(t), \quad t = 0, 1, \ldots, N-1. \tag{21}$$

The acceleration in (21) is a_2 rads/sec^2, whereas the instantaneous frequency (IF) is $(2a_2 t + a_1)$ rads/sec. The 2nd-order moment of $x(t)$ at lag 1 is given by

$$z(t) := E[x(t)x^*(t-1)] = c_{2s}(1)e^{j2a_2 t}e^{j(a_1 - a_2)} + c_{2v}(1), \tag{22}$$

where $c_{2s}(1) := E[s(t)s^*(t-1)]$ and similarly for $c_{2v}(1)$. Apparently, $z(t)$ is a constant amplitude harmonic process at frequency $2a_2$. In practice, one estimates (22) via the so-called ambiguity function (AF) (e.g., [2]), defined as $\hat{z}(t) := x(t)x^*(t-1)$, and then obtains $2a_2$ from any of the frequency estimation schemes (e.g., FT, MUSIC). Once a_2 is found, one demodulates $x(t)$ by $\exp\{-ja_2 t^2\}$, and obtains

$$\tilde{x}(t) := x(t)\ e^{-ja_2 t^2} = s(t)\ e^{ja_1 t} + v(t)\ e^{-ja_2 t^2}. \tag{23}$$

Under the high SNR condition **(a2)**, (23) approximates the random amplitude harmonic model in (1), and a_1 can be estimated as usual.

4. EXPERIMENTAL RESULTS

We provide here some simulated as well as real data examples to illustrate the algorithms developed in this paper.

Example 1: Since the "ground truth" of a storm is often not available, it is difficult to compare estimation algorithms using real data. The method of [9] for generating weather-like signals has been useful in evaluating various algorithms, since one knows the "truth". Figs. 1a and 1b show respectively the in-phase (I) and quadrature (Q) component of a simulated weather radar signal, whose true PSD is shown in Fig. 1c. The spectrum of $s(t)$ is bell-shaped generated according to $S_s(\omega) = 10/\sqrt{2\pi}\ \exp\{-50\omega^2\}$, whereas the spectrum of $v(t)$ is non-flat as in $S_v(\omega) = [12.5 - 10\cos(\omega)]^{-1}$. The Doppler shift ω_0 was chosen to be 1.5. The MUSIC pseudo-spectrum is shown in Fig. 1d which peaks around ω_0. The mean$\pm$std of $\hat{\omega}_0$ obtained from 100 independent realizations were 1.0995 ± 0.1413 for the PP processor, and 1.4941 ± 0.0335 for the MUSIC algorithm. The latter is seen to be robust to colored $v(t)$.

Example 2: 128 samples of radar data were collected from a rain storm occurred in Norman, OK, on June 10, 1994. Figs. 2a and 2b plot the I, Q components, and Fig. 2c shows the PSD estimate. Since the spectrum is single modal and bell-shaped, the PP processor yielded $\hat{\omega}_0 = 1.4359$ which can be regarded as reliable. Fig. 2d plots the MUSIC pseudo-spectrum which peaks at 1.4421, and agrees very well with the estimate from the PP processor.

Example 3: Fig. 3a/b shows 32 samples of the I/Q component of lidar data collected under fair weather conditions. Fig. 3c illustrates the PSD estimate. The presence of the secondary peak leads us to believe that the estimate $\hat{\omega}_0 = -0.1961$ obtained from the PP processor must be biased. The MUSIC pseudo-spectrum is plotted in Fig. 3d whose peak location at $\hat{\omega}_0 = -0.7316$ is close to that indicated by the PSD. Note that the power-weighted mean frequency estimate (the centroid of the PSD) [3, p. 131], will also be biased in the presence of the secondary peak.

Example 4: We demonstrate here the AF approach for estimating time-varying wind velocity. In this particular case, the wind velocity is decreasing which may be due to the direction of the wind turning away from the line-of-sight of the laser beam. The estimate of the IF obtained from the short-time FT (STFT) is depicted in Fig. 4a whereas the AF approach yielded the IF profile as shown in Fig. 4b. The acceleration was estimated to be -0.024 rad/sec^2. Note that one can always perform a linear least squares fit to Fig. 4a in order to obtain an acceleration estimate. However, such a multi-stage procedure is computationally more involved. Further, it relies on the STFT estimates, which could be subjective when it comes to choosing appropriate window lengths and the amount of overlap.

Acknowledgments: The authors thank Dr. D. S. Zrnić of the National Severe Storms Lab. of NOAA at Norman, OK, and Simpson Weather Associates of Charlottesville, VA, for providing the radar and lidar data used in this paper.

REFERENCES

[1] D. R. Brillinger, *Time Series: Data Analysis and Theory*, Holden-day Inc., San Francisco, 1981.

[2] P. M. Djurić and S. M. Kay, "Parameter estimation of chirp signals," *IEEE Trans. ASSP*, vol. 38, pp. 2118-2126, 1990.

[3] R. J. Doviak and D. S. Zrnić, *Doppler Radar and Weather Observations*, Academic Press, 2nd edition, 1993.

[4] S. Haykin, *Adaptive Filter Theory*, 2nd ed., 1991.

[5] R. A. Horn and C. A. Johnson, *Matrix Analysis*, 1985.

[6] L. H. Janssen and G. A. Van Der Spek, "The shape of Doppler spectra from precipitation," *IEEE Trans. on Aerospace & Electronic Systems*, vol. 21, pp. 208-219, 1985.

[7] J. Klostermeyer, "Maximum entropy estimation of Doppler shift and spectral width of VHF radar signals," *Radio Science*, vol. 24, pp. 47-63, 1989.

[8] R. T. Menzies and R. M. Hardesty, "Coherent Doppler lidar for measurements of wind fields," *Proceedings of the IEEE*, vol. 77, pp. 449-462, 1989.

[9] D. S. Zrnić, "Simulation of weatherlike Doppler spectra and signals," *J. of Appl. Meteorology*, vol. 14, pp. 619-620, 1975.

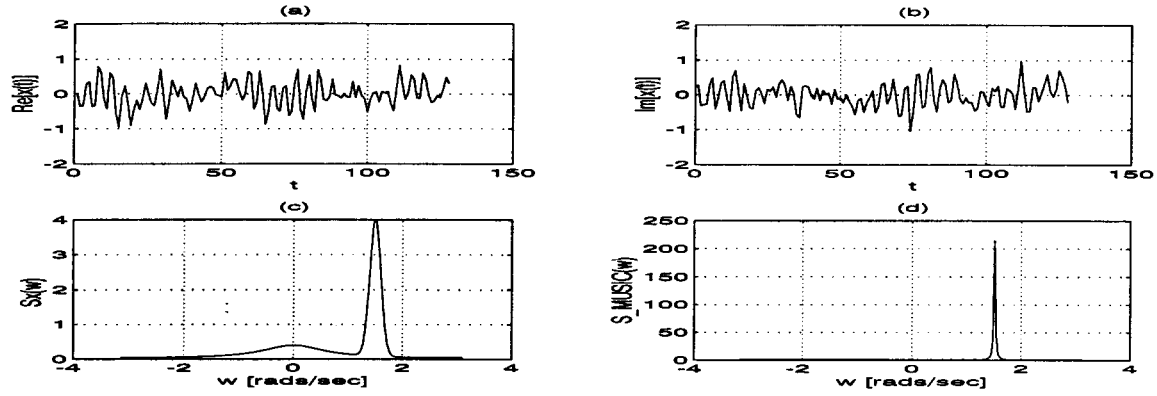

Figure 1. Simulated weather radar signal, PSD, and MUSIC pseudo-spectrum

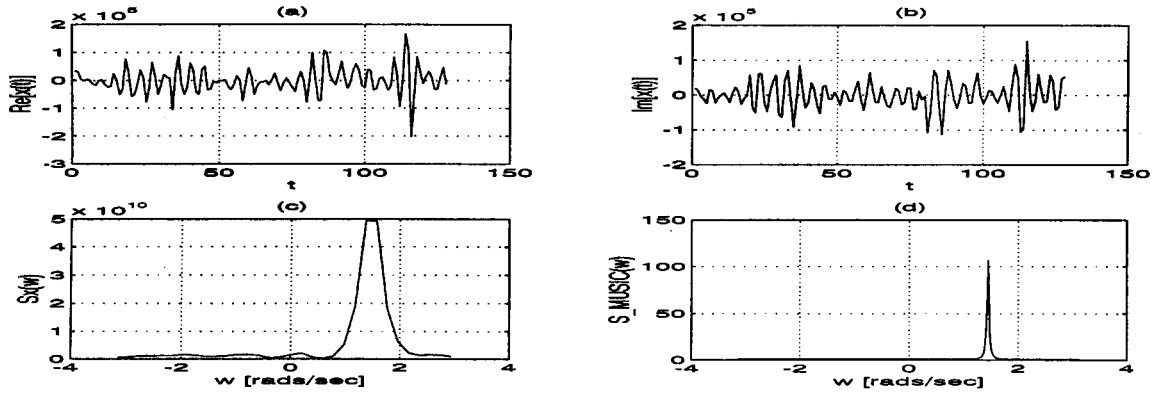

Figure 2. Real weather radar signal, PSD, and MUSIC pseudo-spectrum

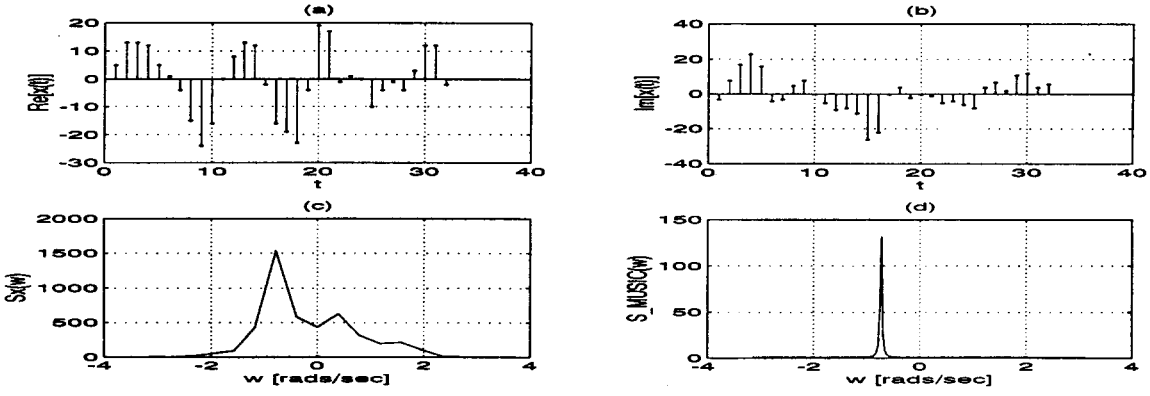

Figure 3. Real weather lidar signal, PSD, and MUSIC pseudo-spectrum

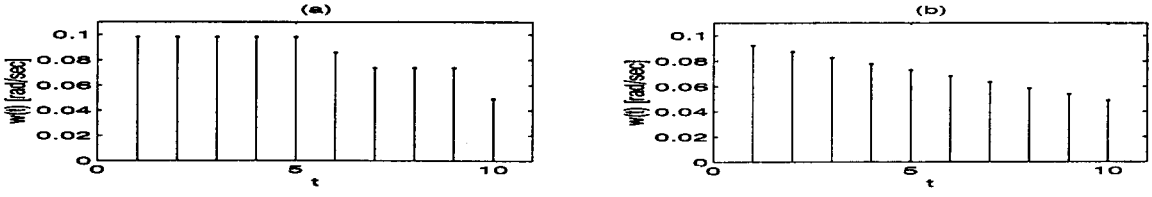

Figure 4. IF estimates from STFT and ambiguity function for weather lidar observations